JTTEE5 9:215-224




# Three-Dimensional Simulation of Thermal Plasma Spraying of Partially Molten Ceramic Agglomerates

*I. Ahmed and T.L. Bergman*

*(Submitted 31 March 1999; in revised form 6 December 1999)*

**Thermal plasma spraying of agglomerated nanostructured ceramic particles has been studied using computational fluid dynamics. The plasma jet is modeled as a mixture of Ar-$H_2$ plasmas issuing into a quiescent atmosphere. The particles, modeled as micron-sized spheres, are introduced into the jet outside the plasma gun exit with radial injection. The existence of a simple target in front of the plasma gun is taken into account. The trajectories and state histories of particles of various sizes during their flight through the jet are presented. Moreover, the solid-liquid interface within the particles is tracked in an attempt to predict the amount of unmelted material retained in these particles at various axial distances from the gun exit. The effects of turbulence in the jet on these particle histories are accounted for. It is shown that, for the range of particle sizes and the plasma gun operating conditions studied, both the deposition location and the retained unmolten fraction are strongly affected by the size of the particles. The predictions are significant in terms of showing general trends, which will be useful in identifying processing windows for producing optimally nanostructured coatings.**

**Keywords** nanostructured ceramics, melting and resolidification, computational fluid dynamics, stochastic deposition patterns

## 1. Introduction

Thermal spraying of micron-sized metallic and ceramic powder particles onto metallic substrates is an important process in modifying surface properties of engineered components. Due to the ever-increasing application as well as the widening range of properties demanded of these coatings, a deeper understanding of the process and its controlling parameters has become essential. A recent innovation in coating technology has been the proposed use of agglomerated nanostructured ceramic as well as metallic carbide particles. Nanostructured coatings may provide additional insulation, corrosion, and wear resistance, as well as better surface finish and other useful features not yet fully characterized.[1,2]

In conventional plasma spraying, the adhesion of the coating material to the substrate is achieved by melting the powder in the hot gases. For plasma spraying of nanostructured materials, the current thinking is that some of the sprayed material must be in a molten state at the moment of impact to provide the necessary bonding mechanism. However, some of the sprayed material must remain not only solid, but should never be sintered or liquefied in its flight in order to achieve a coating with retained nanostructure. Thus, in order to achieve the maximum deposition efficiency along with the optimum nanostructure, a very narrow processing window may need to be identified.

**I. Ahmed,** Institute of Materials Science, and **T.L. Bergman,** Department of Mechanical Engineering, The University of Connecticut, Storrs, CT 06269-3139.

Experimental observation of thermal plasma spraying processes remains difficult. Therefore, to facilitate understanding of the plasma-particle interaction, computational or numerical simulation has been used extensively with various degrees of success. The simplest geometric configuration has been a two-dimensional axisymmetric jet, with particles injected into the stream (one at a time) in order to study their heating and acceleration (see, for example, the predictions made in Ref. 3 and 4). Three-dimensional (3-D) simulations are beginning to appear in the literature as the need continues for more realistic modeling of 3-D effects associated with the transverse injection of particles.[5]

Here, the thermal plasma spraying process has been simulated using a commercial computational fluid dynamics package, FLUENT,[6] which is coupled to an original model to predict the instantaneous state of individual injected particles. Specifically, a fully 3-D simulation of a plasma jet with transverse injection of nanostructured particles, as well as its interaction with a stationary target, is reported in this article.

The particles are modeled as spheres with constant properties, and the possibility of melting and resolidification of these particles is included in the model description. Since the focus of this study is agglomerated nanoparticles (which can be either solid or hollow with a porous shell), hollowness of the particle is also considered. Particle trajectories and temperature histories are predicted in conjunction with a stochastic model, which takes into account the effects of turbulent fluctuations in the jet. Possible nanostructure retention as well as the deposition pattern (footprint) on the target has been studied as a function of particle size and hollowness.

## 2. Computational Modeling

Steady-state gas phase calculations were performed in conjunction with a transient simulation of melting and resolidification of injected particles. These are injected radially into the jet

**Table of Symbols**

| | | | |
|---|---|---|---|
| $c$ | specific heat J/kg·K | $r$ | radial coordinate(s), inside a spherical particle, or in the cylindrical computational domain for the plasma jet |
| $C_D$ | coefficient of drag force, $= \frac{F_D}{\frac{1}{4}\pi D^2 \times \frac{1}{2}\rho U^2}$ | $r_{in}$ | inner radius of powder particles ($\neq 0$ for hollow particles) |
| $D$ | particle diameter, $\mu$m | $r_{out}$ | outer radius of powder particles |
| $f_L$ | liquid fraction of particle volume, instantaneous | $Re_D$ | Reynolds number based on plasma-particle relative speed $= \frac{\rho UD}{\mu}$ |
| $f_{RN}$ | retained nanostructured fraction of particle volume | $s$ | solid phase |
| $f_S$ | instantaneous solid fraction | $t$ | time, s |
| $F_D$ | fluid drag force on particle, $N$ | $T$ | temperature, K |
| $h$ | average heat-transfer coefficient, W/m²·K, between particle and surrounding gas | $T_f$ | fusion temperature of ceramic material, K |
| $H$ | internal energy of particle material, J/kg | $x$ | axial coordinate |
| $\Delta H_f$ | latent heat of fusion of particle material, J/kg | $u, v, w$ | velocity components in the fluid phase, m/s |
| $k$ | thermal conductivity, W/m·K; turbulent kinetic energy, m²/s² | $U$ | relative speed between particle and (local) fluid, m/s |
| $l$ | liquid phase | $\epsilon$ | emissivity; turbulent energy dissipation rate, m²/s³ |
| $n$ | nanostructured material | $\iota$ | phase change temperature interval, K (used in the *enthalpy formulation*) |
| $Nu_D$ | Nusselt number, $= \frac{hD}{k}$ | $\mu$ | fluid phase viscosity, kg/m·s |
| Pr | Prandtl number, for fluid, $= \frac{\mu c}{k}$ | $\rho$ | density, kg/m³ |
| | | $\sigma$ | Stefan-Boltzmann constant, $5.67 \times 10^{-8}$ W/m²·K⁴ |

**Subscripts**

| | | | |
|---|---|---|---|
| $p$ | particle material properties | $s$ | particle surface |
| gas | fluid phase properties | $\infty$ | surrounding surface |

and sprayed toward a stationary, cooled target. The plasma was simulated as a turbulent jet of a mixture of argon and hydrogen plasmas issuing into quiescent ambient air.

Because of the radial injection of the particles, and the existence of a stationary target, which is cooled from the back side, 3-D elliptic calculations (gas velocities can occur in any positive or negative direction) must be performed. FLUENT is a control volume based fluid dynamics code that uses the SIMPLE algorithm[7] to solve the 3-D, elliptic form of the Navier-Stokes equations. Because 3-D, elliptic simulations are very expensive relative to the parabolic (velocities in positive coordinate directions only) models that are typically used in thermal spray simulation, chemical reactions were not taken into account to avoid excessive CPU time and memory requirements. This simplification has been made by others who have performed recent 3-D simulations of the plasma spraying process.[8,9] To our knowledge, 3-D elliptic calculations which include chemical reactions have not been attempted.

In our simulations, the conservation principles of momentum, energy, and chemical species are applied. Three nonreacting species (argon, hydrogen, and air) are accounted for. Viscous dissipation is neglected. Although the present simulations do not account for chemical reactions, which may be significant,[3,4,10] the estimate of the excess energy released from the chemical reactions accounts for less than 10% of the total energy available for particle heating. It should also be noted that chemical reactions may also affect the composition of the gases and, in turn, the transport properties of the gases. Other assumptions have been made regarding the momentum exchange between the gas and the particles, including the neglect of non-continuum effects, Basset history, as well as the possible impact of thermophoresis in determining the trajectories of the particles. The last three effects have been deemed to be small by a number of authors as discussed in Ref 4 and 11. Likewise, there is considerable uncertainty regarding the proper method to model the arc instabilities developed within the plasma gun.[12] Here, the instabilities are treated as a high level of turbulence existing at the jet exit.

### 2.1 Plasma Jet Simulation

The various temperature-dependent transport and thermodynamic properties of the plasma were obtained from data calculated on the basis of local thermodynamic equilibrium.[13] The atmospheric air was treated as a single species with known properties. The plasma-air mixture properties, however, were calculated on a mole-fraction basis. The density of the gas mixture was calculated from the *ideal gas law*.

**Turbulence Modeling.** To describe the turbulence effects, the $k$-$\varepsilon$ model was employed, along with its renormalization group theory extension.[14] The high fluctuations in the flow exit conditions (caused by arc instabilities inside the gun) were modeled by prescribing a turbulence intensity level of 20% at the gun exit; this value resulted in predicted deposition patterns that are similar to those observed in specimens sprayed by one of the authors (I.A.).

**Operating Condition Parameters.** The fluid flow calculations were performed on a polar-cylindrical grid of 24 (axial) × 24 (radial) × 32 (angular) cells. Additional cells (in the axial direction) were included to incorporate a disk-shaped target, and a backside cooling jet set close behind the target (Fig. 1).

The plasma jet exit diameter is 8 mm, and the target stands 97 mm (=$L_{stdf}$) away from the jet with its axis coincident with that of the jet. The target is 24 mm in diameter and 3 mm thick. The Ar-$H_2$ (80:20 by volume) plasma exit velocity and temperature are 300 m/s and 12,000 K, respectively, both exiting profiles being flat. The target backside cooling is modeled by a jet of air situated 20 mm behind, again with flat velocity and temperature profiles, at 300 K and 10 m/s, respectively.

At the outer boundary of the computational domain, *free boundary conditions* were imposed. This means that, in regions where ambient air is entrained into the computational domain, the total pressure (standard atmospheric), temperature (300 K), and turbulence level (1%) are specified. In regions where plasma-air mixture flows out of the domain, zero gradients (normal to the flow) are assumed for all the relevant variables. The density of all the fluid species (plasma components as well as air) is modeled with the ideal gas law. Transport properties of the mixture were calculated on a mole-fraction basis, and the specific heat was determined on a mass-fraction basis.

### 2.2 Plasma-Particle Interaction

The nanostructured particles are injected numerically into the plasma-air mixture stream that is predicted using the plasma jet simulation model. Particle tracking was achieved using an Eulerian-Lagrangian scheme. The local instantaneous drag force ($F_D$) of the plasma-air mixture on the particles determines the trajectory of each particle:

$$m_p \frac{d\bar{u}_p}{d\bar{t}} = \bar{F}_D \qquad \text{(Eq 1)}$$

The value of $F_D$ was calculated on the basis of *Stokes' law* for low-Re flow over a sphere:

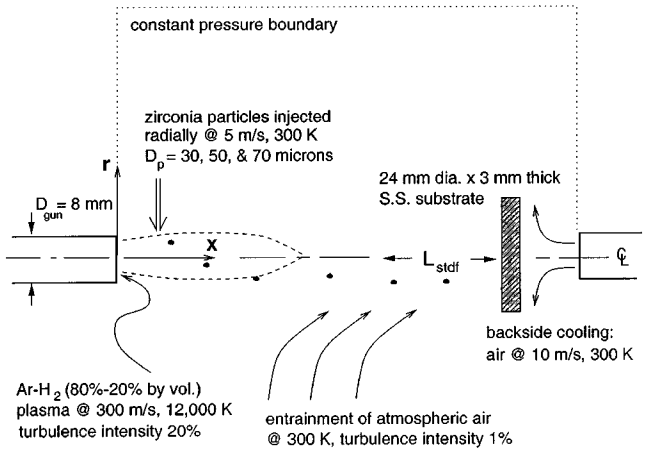


**Fig. 1** A schematic representation of the plasma spraying gun and target with the injection point of powder particles shown

$$C_D = \frac{24}{\mathrm{Re}_D} \qquad \text{(Eq 2)}$$

**Stochastic Trajectories.** The particle trajectories were calculated with the assumption that turbulent eddies have lifetimes of random values. This assumption leads to the (realistic) prediction that random variations occur in the instantaneous drag force upon a particle as it passes through each of these eddies. In calculating the turbulent fluctuations in the (fluid phase) velocity components, a normal distribution was assumed:

$$u' = \zeta\sqrt{u'^2} \qquad \text{(Eq 3)}$$

where $\zeta$ is a randomly generated number. The turbulent kinetic energy, $k$, was assumed to be equally partitioned in all three components (isotropic turbulence):

$$\sqrt{\overline{u'^2}} = \sqrt{\overline{v'^2}} = \sqrt{\overline{v'^2}} = \sqrt{2k/3} \qquad \text{(Eq 4)}$$

In the trajectory predictions presented here, particle-particle interaction (such as collision) was not considered. Particle loading effects on the jet were not included either, thereby limiting the predictions to cases where the ratio of particle to gas mass flow rates is less than 10%.[11]

**Solid-Liquid Front Tracking Inside Sprayed Particles.** The thermal phenomenon inside each particle, along with solid-liquid phase change, was predicted with an original user-defined code linked to FLUENT. The algorithm for this calculation was based on the *enthalpy method*.[15] The particles, along with the temperature variations inside each of them, were assumed to be spherically symmetric. This reduced the problem description to one dimension:

$$\frac{\partial H}{\partial t} = \frac{1}{r^2}\frac{\partial}{\partial r}\left(kr^2\frac{\partial T}{\partial r}\right) \qquad \text{(Eq 5)}$$

$$H = \begin{cases} \rho c\left(T - T_f\right), & T < T_f \\ f_L \rho \Delta H_f, & T_f < T < T_f + \iota;\ 0 < f_L < 1 \\ \rho \Delta H f + \rho c\left(T - T_f\right), & T > T_f + \iota \end{cases} \qquad \text{(Eq 6)}$$

with the reference internal energy, $H_{ref} = 0$ at $T = T_f$, and $i = 10^{-6}$ K. An equilibrium model was employed for the phase change phenomena. Such a model has been found to be sufficient for particle melting phenomena in a recent work that examined predictions from both the equilibrium and kinetic nonequilibrium models.[4] An explicit time-integration scheme was employed. The boundary conditions for the heat equation applied within the particle were

(at $r = r_{in}$)

$$\frac{\partial T}{\partial r} = 0 \qquad \text{(Eq 7)}$$

(at $r = r_{out}$)

$$-k_p\frac{\partial T}{\partial r} = h\left(T_s - T_{gas}\right) + \varepsilon\sigma\left(T_s^4 - T_\infty^4\right) \qquad \text{(Eq 8)}$$

The first boundary condition is straightforward. The boundary condition at the outer radius takes into account both convective heat transfer to the surrounding gases ($T_{gas}$ being the average temperature of the fluid surrounding the particle) and diffuse gray radiative exchange with the environment, which was assumed to be a large surrounding at 300 K. The turbulent fluctuations in the gas phase temperature field were neglected. Although there is uncertainty regarding the value of $\varepsilon$, the radiative component of the heat flux at the surface is typically less than 1% of the total, as also noted in Ref 4. Radiation effects *within* the particles were neglected.

The convective heat transfer coefficient was computed from correlations for droplets:[16]

$$\mathrm{Nu}_D = 2 + 0.6\,\mathrm{Re}_D^{\frac{1}{2}}\,\mathrm{Pr}^{\frac{1}{3}} \qquad \text{(Eq 9)}$$

For further details on fluid flow simulation as well as plasma-particle interaction, the reader is referred to the *FLUENT User's Guide*[6] and the references contained therein.

## 3. Results

The predicted axial variation of the plasma velocity ($x$ component), temperature, and species concentration (argon) is presented in Fig. 2. A quantitative comparison with similar data found in the literature (for example, Refs 3, 8, 17, and 18) is impossible because of the probable mismatch in jet exit conditions in terms of plasma jet species composition, velocity and temperature distribution, and, above all, turbulence quantities. However, qualitative agreement has been found with data available in the references. The decay in all three quantities presented along the axis is typical (Fig. 2).

Zirconia particles of 30, 50, and 70 $\mu$m diameter are injected radially inward with an initial velocity of 5 m/s at $x$ = 5 mm (from the jet exit) and $r$ = 5 mm (from the jet axis). The initial temperature of all particles is 300 K. Thermophysical properties of the powder particle material have been taken from various sources[19,20,21] and are summarized in Table 1. Note that the actual properties of the agglomerated nanoparticles probably differ somewhat from those listed in Table 1, which are for dense zirconia; actual properties of agglomerated nanostructured zirconia are not yet available.

### 3.1 Predictions based on the Mean Flow Field

The *mean* trajectories (*i.e.*, trajectories predicted without any randomness) of the three solid particles are superimposed on contours of constant turbulent kinetic energy and temperature in Fig. 3. The three mean trajectories confirm the aerodynamic size classification of particles as observed in the experimental studies reported in Ref 22. The terminal point of each of these trajectories at or near the target indicates where to expect the centroid of the footprint of a spray consisting of a single particle size. Further discussion in this regard can be found in the next section.

It may noted that the injection point is close to the edge of the jet, where turbulent mixing is the most active in entraining ambient air. The temperature is not the maximum near the injection point, however, and it can be seen upon close inspection that the 30 $\mu$m particle is the least exposed to the hot gases. In contrast, the 70 $\mu$m particle passes through the hot axis of the jet.

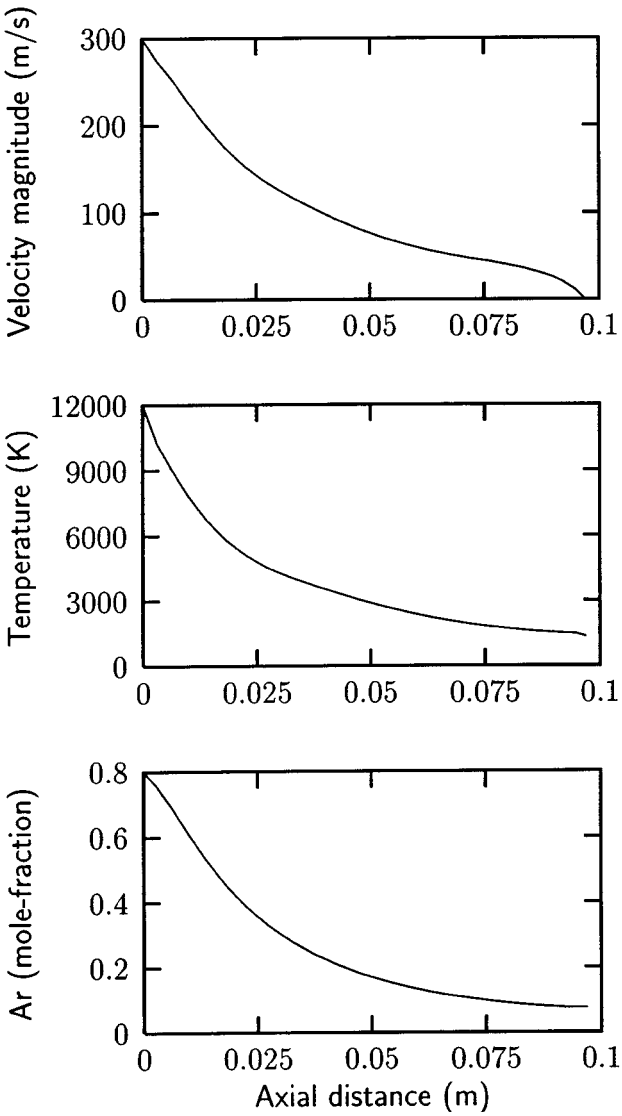


**Fig. 2** Axial variation of velocity magnitude, temperature, and Ar concentration of the plasma jet calculated

**Table 1 Thermophysical properties of zirconia (powder particles) and stainless steel (substrate target) used in the current simulations[19,20,21]**

| | | | |
|---|---|---|---|
| **Zirconia (dense form)** | | | |
| ρ | 5700 kg/m$^3$ | $\Delta H_f$ | $7 \times 10^5$ J/kg |
| $c$ | 620 J/kg·K | $T_f$ | 2980 K |
| $k$ | 2.4 w/m·K | $\varepsilon$ | 0.35 |
| **Stainless steel** | | | |
| $k$ | 25.4 w/m·K | $\varepsilon$ | 0.25 |

### 3.2 Stochastic Trajectories and Deposition Patterns

The simulations for each of the three sizes of particles were repeated, but with the stochastic model enabled to account for turbulent fluctuations. A total of 300 particles were injected. A summary of the statistics is presented in Table 2.

**Table 2 Summary of stochastic particle trajectories presented in terms of the geometry of spray footprint on the target: for 300 (=N) parties of each size, the distance of the corresponding footprint centroid from the injection point, $\bar{d} = (\bar{y}^2 + \bar{z}^2)^{1/2}$, where $\bar{y} = \frac{\sum y_i}{N}$, *etc.;* and the degree of dispersion, $d_\sigma^2 = \frac{\sum (y_i - \bar{y})^2 + (z_i - \bar{z})^2}{N}$ [here, $y_i$ and $z_i$ are the vertical and horizontal distances (perpendicular to the gun axis), respectively, of each deposition location from the injection point]**

| $D$ | ($\mu$m) | 30 (solid) | 50 (hollow) | 50 (solid) | 70 (solid) |
|---|---|---|---|---|---|
| $\bar{z}$ | (mm) | –0.25 | –0.12 | –0.02 | –0.09 |
| $\bar{y}$ | (mm) | –9.49 | –12.83 | –13.59 | –17.85 |
| $\bar{d}$ | (mm) | 9.49 | 12.83 | 13.59 | 17.85 |
| $d_\sigma^2$ | (mm$^2$) | 5.65 | 3.81 | 3.30 | 2.74 |
| $\frac{\bar{d}}{D}\frac{\rho}{\rho_{app}}$ | (—) | 316 | 293 | 272 | 255 |
| $d_\sigma^2 D \frac{\rho_{app}}{\rho}$ | (mm$^3$) | 0.17 | 0.17 | 0.17 | 0.19 |

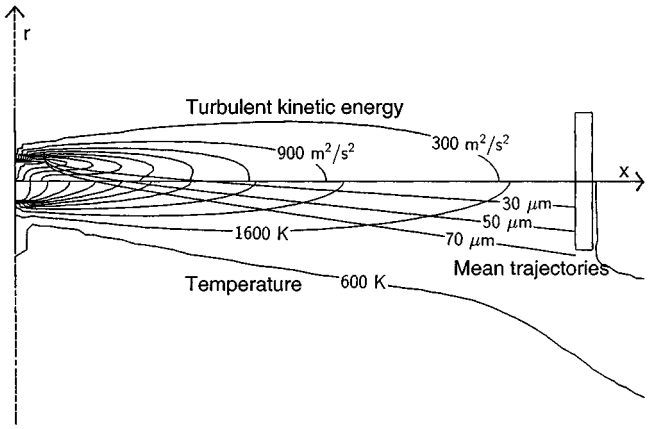


**Fig. 3** Mean trajectories of three particles sizes ($D$ = 30, 50, and 70 $\mu$m) superimposed on the plasma jet flowfield, which is axisymmetric because of the absence of either carrier gas injection or loading effects. The top half of the figure shows turbulent kinetic energy varying from 300 to 5100 m$^2$/s$^2$ (near the jet exit), in intervals of 600 m$^2$/s$^2$; the bottom half shows temperature variations, from 600 to 10,600 K (near the exit), in intervals of 1000 K

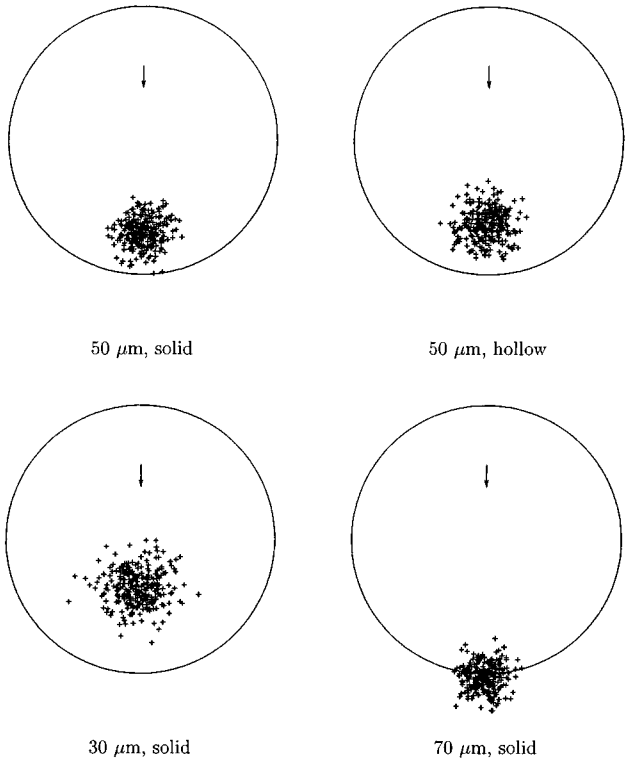


**Fig. 4** Deposition locations for various particles on a 25 mm diameter target: 50 $\mu$m solid and hollow (*top left* and *right*) and 30 and 70 $\mu$m solid particles (*bottom left* and *right*). A sample of 300 particles is shown for each. Note the slightly larger dispersion for the hollow 50 $\mu$m particles as compared with the solid ones of the same size. Furthermore, the 30 $\mu$m particles have the largest dispersion, while the 70 $\mu$m particles are deposited farthest from the injection point. The tips of the arrows indicate the direction as well as the point of injection; the plasma gun's axis passes through the center of this target. See Table 2 for a quantitative analysis of these results

The deposition locations are presented (along with an outline of the target) in Fig. 4. The injection direction and location is identified by the arrowhead. Although all particles have the same initial velocity, by the time they reach the target, they become grouped according to their size and mass. This can again be explained in terms of the differences in the drag forces experienced by the particles of different sizes, and also the different momentum each size carries due to its mass. The smaller (lighter) particles are not able to penetrate as far into the plasma core, and reach the target at the highest locations. The larger (heavier) particles cross the plasma axis quite early—passing through the core area—and hit the target at its lowest locations. (In fact, most of the larger particles miss this particular target, as was indicated by the corresponding *mean* trajectory in Fig. 3). Furthermore, the relative dispersion in the deposition pattern (due to turbulence effects) is higher for the smaller (lighter) particles, as expected.

For the 50 $\mu$m hollow particles, the dispersion in the deposition pattern is slightly larger than that for the solid particles of the same size. This is due to the hollow particles' lower average density, which makes them more susceptible to the randomness of the turbulent jet. Since they carry with them a smaller momentum at injection, the centroid of the deposition pattern is also slightly closer to the axis of the target.

For the particular combination of plasma gun exit conditions, stand-off distance, and the particles used in this study, it is possible to correlate the average deflection ($\bar{d}$, see Table 2 for

definition) with the particle size (the apparent density, $\rho_{app}$, is taken into account for the hollow particles), with an average value of $(\bar{d}/D)(\rho/\rho_{app}) = 284$. Another strong correlation is found between the degree of dispersion ($d_\sigma^2$) resulting from the turbulent fluctuations in the jet, and the particle size, with an average value of $(d_\sigma^2 D)(\rho/\rho_{app}) = 0.17$ mm$^3$.

### 3.3 Mean Plasma-Particle Heat Transfer

The surface temperature variations in the spray are compared for the three particle sizes studied here in Fig. 5. The results correspond to the *mean* trajectories presented in Fig. 3. As noted previously, because of the transverse injection, the trajectories of different particle sizes are different, and each size is exposed to the various parts of the jet core for different lengths of time.

The internal temperature distributions for each particle size at various axial locations during their mean trajectory are presented in Fig. 6. The outer part of the 50 $\mu$m particle begins to melt at $x \approx 15$ mm and remains molten at $T_f = 2980$ K for a large part of the trajectory; the maximum surface temperature is reached at $x \approx 20$ mm, after which the surface begins to cool. The rate of cooling is slow since there is very little heat transfer due to the low-temperature, low-conductivity gas mixture outside the core of the jet.

The 70 $\mu$m particle is heated until $x \approx 25$ mm, and once outside the jet core, the particle is in a low-conductivity medium and the cooling process is very slow. Interestingly, the surface of this larger particle never reaches $T_f = 2980$ K. At the other extreme, the 30 $\mu$m particle melts at the surface at $x \approx 9$ mm, and since the small particle has the lowest heat capacity, it melts completely and is superheated until $x \approx 30$ mm, after which it begins to cool but remains molten until impact.

**Retained Nanostructure in Solid Particles.** As indicated previously, the average 30 $\mu$m particle begins to melt early and remains completely molten for the rest of its flight. The typical 70 $\mu$m particle never melts, while the 50 $\mu$m particle melts partially, and the outer part of molten layer solidifies to form a solid crust with some liquid material trapped between the crust and an inner (nanostructured) core. This phenomenon is illustrated in more detail in Fig. 7, where evolution of the radial temperature distribution inside the 50 $\mu$m particle associated with the mean trajectory is shown. Here, the boundary between nanostructured ($n$) and molten ($l$) material inside the particle moves inward until $x \approx 30$ mm, at which point the superheated outer surface has already begun to cool. At $x = 40$ mm, the entire particle becomes nearly isothermal, with the solid-liquid interface

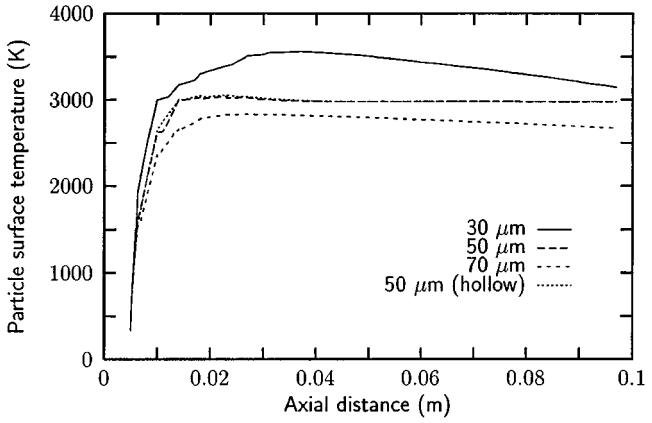


**Fig. 5** The evolution of the surface temperatures of 30, 50 (solid as well as hollow), and 70 $\mu$m particles along their axial locations through the spraying jet. Note that the same axial locations are reached at different times by different sizes of particles due to different accelerations imparted by the jet, and also that the radial positions of each size at the same axial locations are different as well

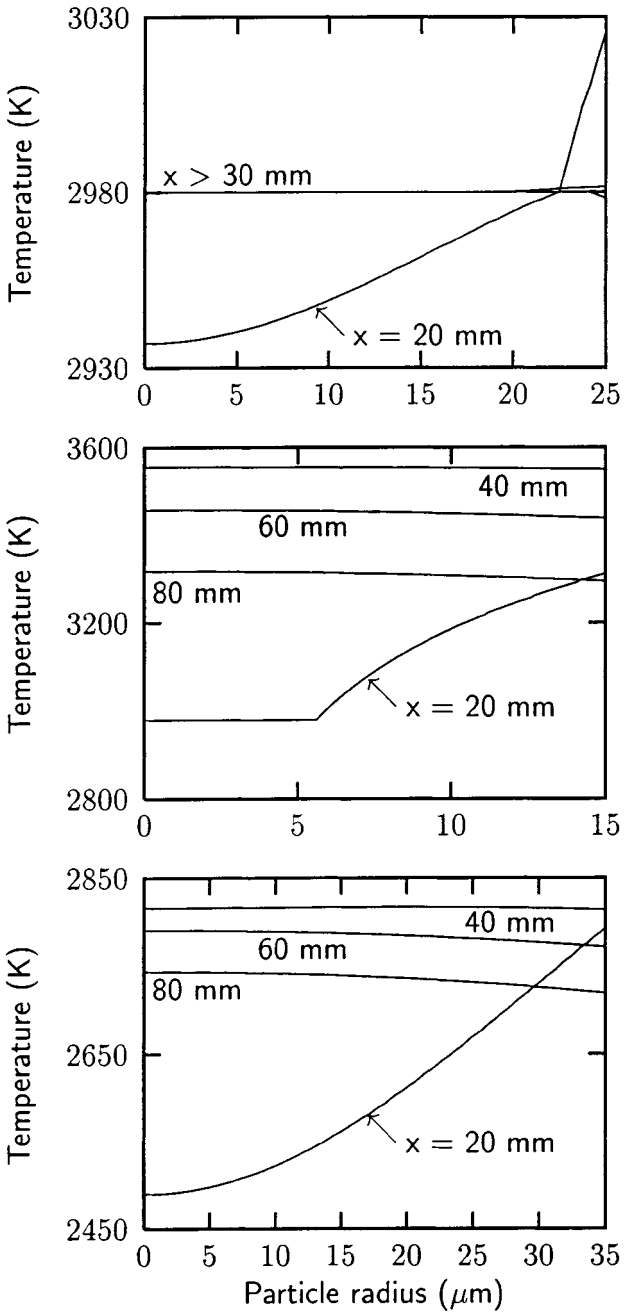


**Fig. 6** The radial temperature profiles inside (*top to bottom*) 50, 30, and 70 $\mu$m solid particles at 20, 40, 60, and 80 mm from the jet exit. For each size, the particles are heated at 20 mm, but have already begun to cool by the time they are at 40 mm. The temperature profiles for the 50 $\mu$m particles after $x = 20$ mm are shown in greater detail in Fig. 7

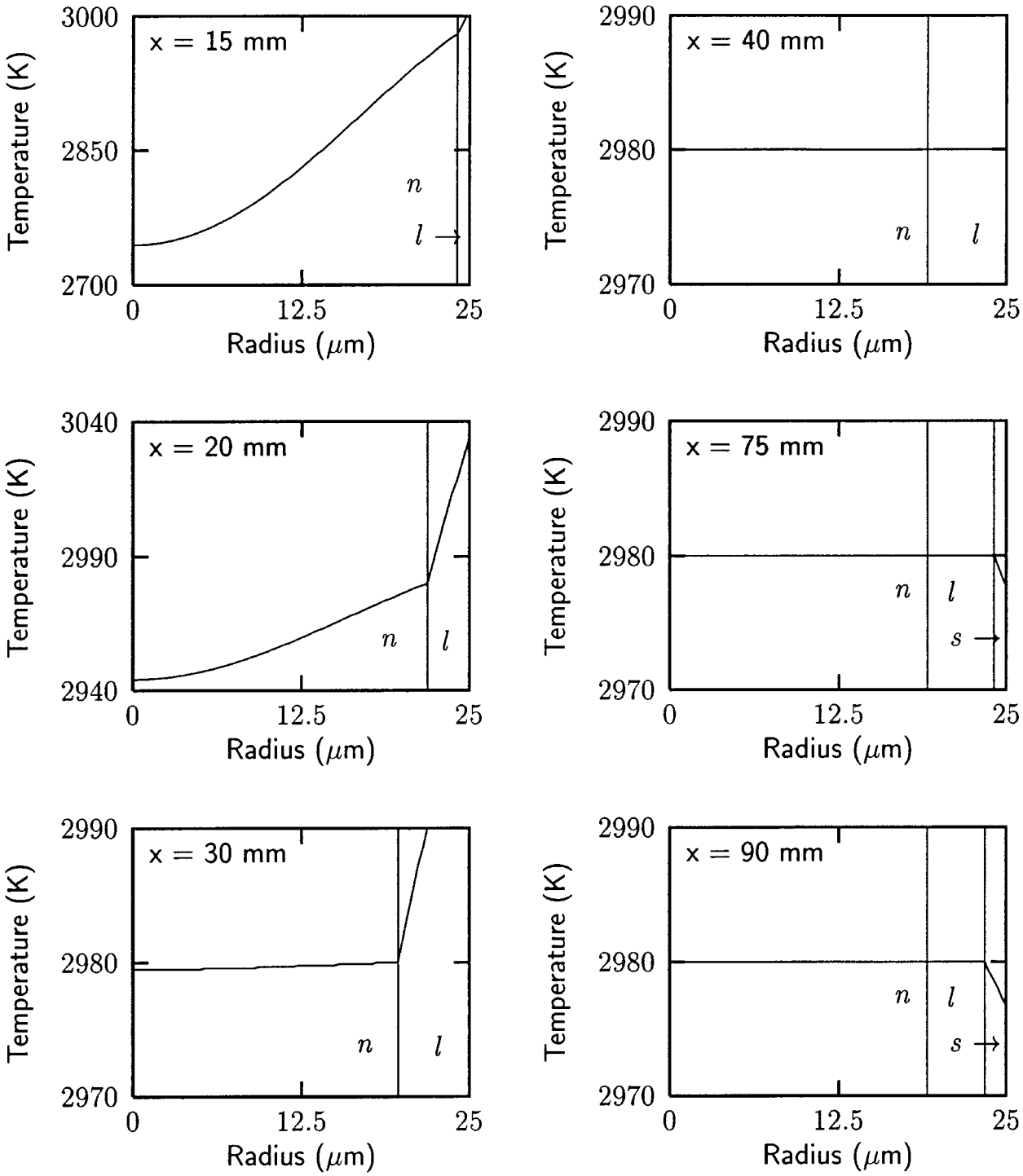


**Fig. 7** Solid-liquid phase-front movement for a 50 $\mu$m solid particle in its flight through the plasma jet (exit temperature: 12,000 K). The locations along the jet axis are 15, 20, 30, 40, 75, and 90 mm (*top to bottom, left to right*). The vertical lines denote the phase interface; toward the end, note the existence of a molten layer trapped between the nanostructured inner core and a resolidifying outer crust

at a standstill due to the absence of any temperature gradient at this interface.

By $x = 75$ mm, the outer layer of molten material has begun to resolidify, forming a solid crust that presumably would have no nanostructure. The crust may also affect the physical mechanisms associated with splat formation and spreading.

**Retained Nanostructure in Hollow Particles.** Agglomerated nanostructured ceramics may also be synthesized with a central void.[11] Here, 50 $\mu$m particles with internal voids of 25 $\mu$m diameter are considered—these have a mass ratio of 0.875 as compared to solid particles of the same outside diameter. The reduced mass results in higher acceleration and faster heating (as well as faster

cooling)—since both the drag force and the heat transfer coefficient are functions of the apparent (outside) diameter.

A solid-liquid front tracking prediction was performed for the hollow particle in the *mean* flow, and the results are in Fig. 8. As expected, because of a lower mass, the inner core reaches $T_f$ = 2980 K as early as $x$ = 30 mm, and the interface continues to move inward until $x \approx 50$ mm, where nanostructured (*n*), molten (*l*), and resolidified (no nanostructure, *s*) material coexist within the particle. Because of the absence of any temperature gradient, the *n*-*l* interface does not move after this point. Therefore, an inner shell of nanostructured material is still possible at impact on a target at $x \approx 100$ mm.

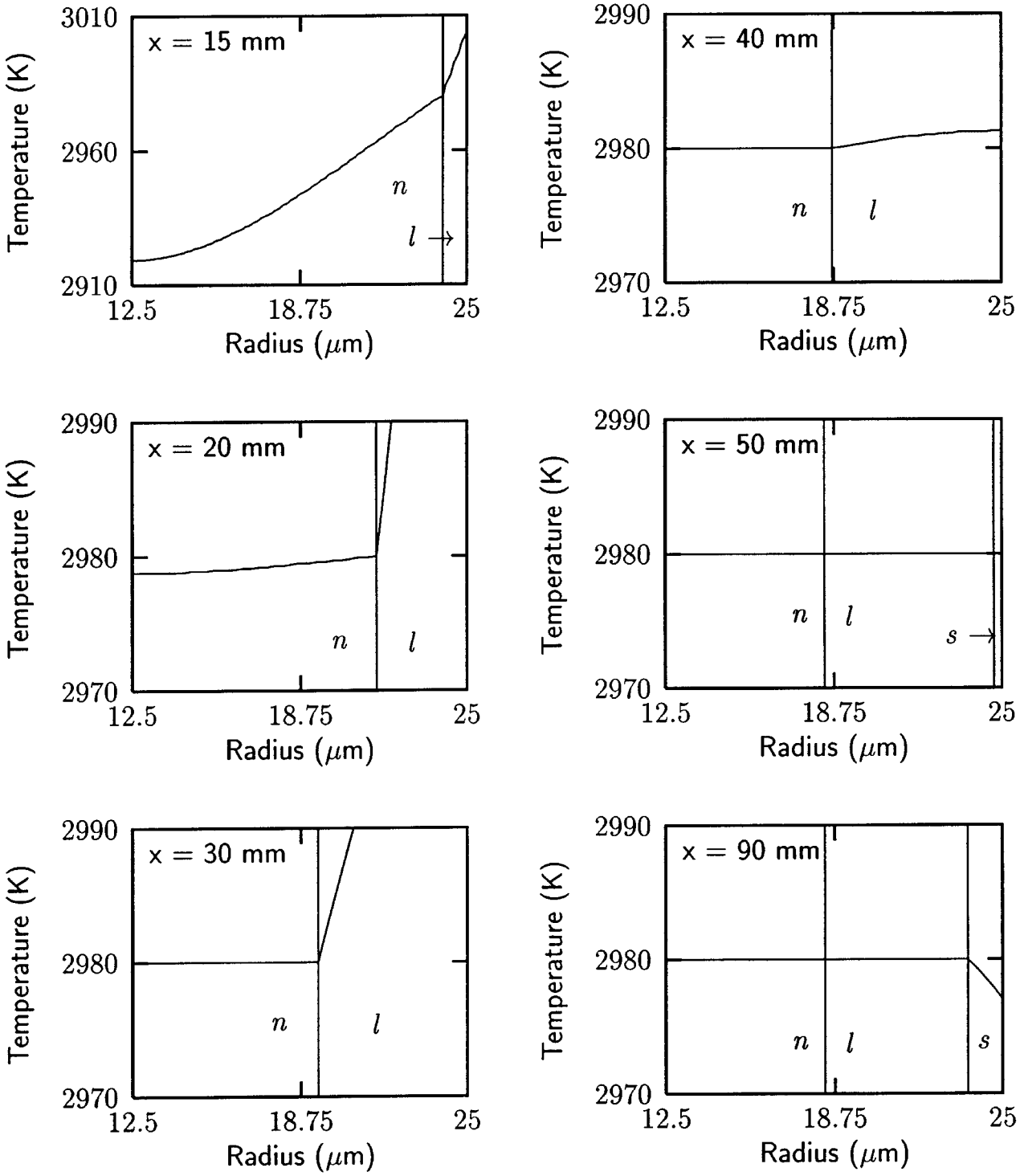


**Fig. 8** Solid-liquid phase front movement for a 50 $\mu$m hollow particle in its flight through the plasma jet (exit temperature: 12,000 K). The locations along the jet axis are 15, 20, 30, 40, 50, and 90 mm (*top to bottom, left to right*). The vertical lines denote the phase interface; once again, note the existence of a molten layer trapped between the nanostructured (hollow) core and a resolidifying outer crust

### 3.4 Stochastic Prediction of Nanostructure Retention

In actual spraying, each particle will be subjected to different gas conditions due to the randomness of the turbulent flow. Different stand-off heights will result in different degrees of nanostructured, liquid, and solid fractions within each particle. The final outcome, *viz.* the coating characteristic(s), will depend upon all these factors. To address these issues, the degree of melting and solidification, as discussed in conjunction with Fig. 7 and 8, was recalculated for the 300 stochastic trajectories for each of the three sizes of particles (as well as for the 50 $\mu$m hollow particles). The calculated average characteristics (of 300 data points at each $x$) do not change appreciably as more trajectories are predicted.

The $f_L$ and $f_{RN}$ values at different axial locations for 50 $\mu$m solid and hollow particles are presented in Fig. 9. Predictions for each of the 300 particles are represented by the data points. Their averaged $f_L$ and $f_{RN}$ values are shown by the lines. As can be seen, solid particles begin to melt at $x \approx 10$ mm, reaching a maximum (instantaneous) molten fraction at $x \approx 40$ mm, after which they begin to resolidify. However, $f_{RN}$ remains constant, since the solid-liquid interface stops advancing inward, and the resolidification at the outer crust cannot reproduce the original nanostructure. An additional curve representing the total fraction of (instantaneous) solid material at any axial location is also presented, which mirrors the $f_L$ variation. The difference between this latter function and $f_{RN}$ values represents the amount of solid material (in the outer crust) that has no nanostructure.

The evolution of $f_L$ and $f_{RN}$ for 50 $\mu$m hollow particles (Fig. 9, bottom) shows similar trends. However, the (relatively) larger loss in $f_{RN}$ is apparent, and is expected. Note that for both solid and hollow (50 $\mu$m) particles, individual particles may undergo melting and resolidification processes that are very different than average behavior (*e.g.*, a few particles undergo complete melting).

Similar predictions for the 30 and 70 $\mu$m particles are presented in Fig. 10. It is interesting to note that the 30 $\mu$m particles melt almost completely by $x \approx 30$ mm and remain molten for the rest of their flight. Hence, no nanostructure is retained. A few particles begin to resolidify near the end of the trajectory ($x \approx 90$ mm). Most of the 70 $\mu$m particles, on the other hand, barely melt, and most retain their original nanostructure. There are, however, some 70 $\mu$m particles that lose all of their nanostructure; the resolidification phenomenon near the end of the trajectory is noticeable as well. Most particles exhibit no partial melting, and no loss in nanostructure; the average evolutions (lines) deviate somewhat from the median trends because of the statistical variations.

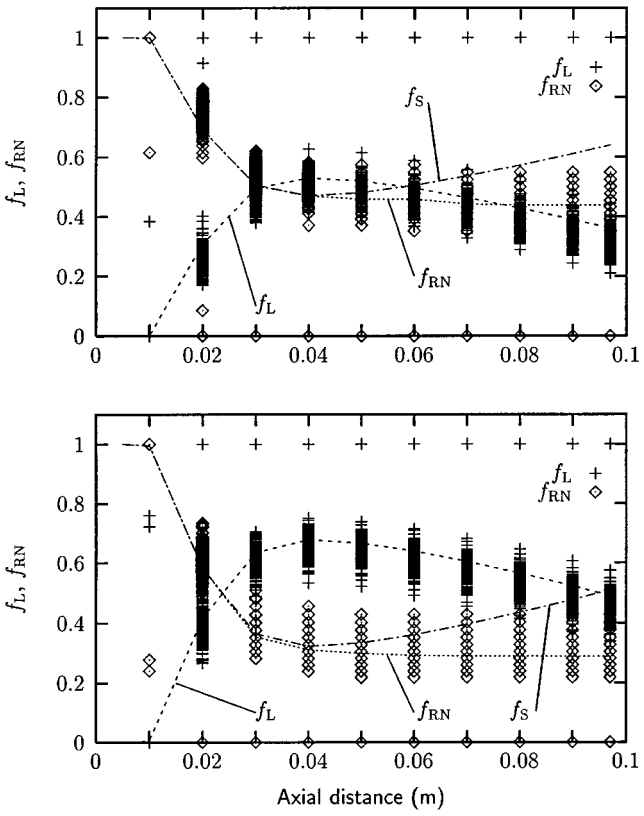


**Fig. 9** The variation in the instantaneous liquid fraction ($f_L$) as well as that in the retained nanostructure ($f_{RN}$) of 50 $\mu$m spherical agglomerates prior to deposition on a target surface 100 mm away: solid (*top*) and hollow (*bottom*) particles. The lines show the calculated average trends of the stochastic variations. The average instantaneous solid fraction ($f_S$) is also shown for comparison with $f_{RN}$ trends ($f_L + f_S = 1$). Note that toward the end of their flight, the liquid fractions begin to decrease from their peak values attained in the "core" of the plasma jet, as the outer parts begin to solidify in a colder surrounding (from this point on, $f_L + f_{RN} < 1$)

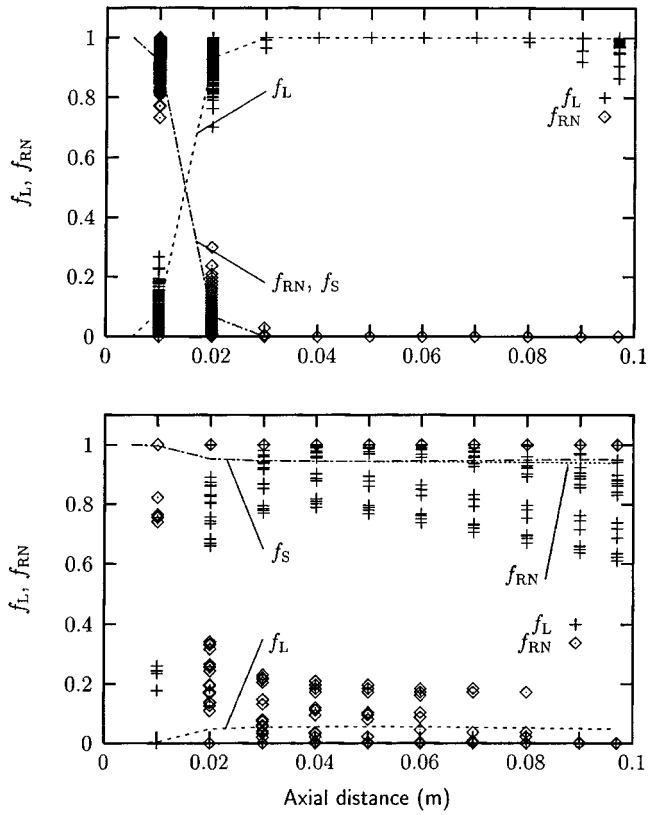


**Fig. 10** The $f_L$ and $f_{RN}$ history of 30 (*top*) and 70 (*bottom*) $\mu$m solid particles in their flights through the plasma jet: most of the smaller particles melted completely, resulting in a total loss of nanostructure, whereas most of the larger particles never melted

## 4. Conclusions

The effects of a turbulent plasma jet on the trajectories and thermal histories of agglomerated nanostructured particles have been studied. The results provide explanations for some of the observations made in recent experiments.[22] More importantly, some key issues for designing further experiments were revealed through these predictions—such as the necessity to tightly control the particle size along with the possibility of defining an optimum stand-off distance for a given power level and gas flow rate of the gun. Further experimental verification of our computational predictions is under way, and once obtained, these predictions will allow us to better identify as well as control the best conditions for spraying an optimally nanostructured coating.

Finally, it should be recalled that the models used in the predictions made here were based on the properties of dense zirconia. These predictions can be further improved when the appropriate data for agglomerated powder particles become available. For example, prediction of interface integrity of the individual subunits (*i.e.,* the original nanoparticles) may be incorporated (with additional modeling) into the analyses presented here.

### Acknowledgments

The work described here is sponsored by the Office of Naval Research, Grant No. N00014-97-0843.

### References

1. B.H. Kear and P.R. Strutt: *Nanostr. Mater.,* 1995, vol. 6, pp. 227-36.
2. M. Gell: *Nanostr. Mater.,* 1995, vol. 6, pp. 997-1000.
3. W.D. Swank, C.H. Chang, J.R. Fincke, and D.C. Haggard: in *Thermal Spray: Practical Solutions for Engineering Problems,* C.C. Berndt, ed., ASM International, Materials Park, OH, 1996, pp. 541-46.
4. Y.P. Wan, V. Prasad, G.-X. Wang, S. Sampath, and J.R. Fincke: *ASME Journal of Heat Transfer,* 1999, vol. 121, pp. 691–6.
5. A. Vardelle, P. Fauchais, B. Dussoubs, and N.J. Themelis: *Plasma Chem. Plasma Processing,* 1998, vol. 18, pp. 551-74.
6. *FLUENT 4.4 User's Guide,* 2nd ed., Fluent Inc., Lebanon, NH, 1997.
7. S.V. Patankar: *Numerical Heat Transfer and Fluid Flow,* Taylor & Francis, Washington, DC, 1980.
8. E. Lugscheider, C. Barimani, P. Eckert, and U. Eritt: in *Progress in Plasma Processing of Materials,* P. Fauchais *et al.,* eds., Begell House, New York, NY, 1997, pp. 871-80.
9. B. Dussoubs, A. Vardelle, and P. Fauchais: in *Progress in Plasma Processing of Materials,* P. Fauchais *et al.,* eds., Begell House, New York, NY, 1997, pp. 861-69.
10. R. Westhoff, G. Trapaga, and J. Szekely: *Metall. Trans. B,* 1992, vol. 23B, pp. 683-93.
11. P. Fauchais, M. Vardelle, A. Vardelle, and J.F. Coudert: *Metall. Trans. B,* 1989, vol. 20B, pp. 263-67.
12. E. Pfender, R. Spores, and W.L.T. Chen: *Int. J. Mater. Prod. Technol.,* 1995, vol. 10, pp. 548-65.
13. B. Pateyron, M.-F. Elchinger, G. Delluc, and P. Fauchais: *Plasma Chem. Plasma Processing,* 1992, vol. 12 (4), pp. 421-48.
14. A. Yakhot and S. A. Orszag: *J. Scientific Computing,* 1986, vol. 1, pp. 1-51.
15. J. Crank: *Free and Moving Boundary Problems,* Clarendon Press, Oxford, United Kingdom, 1984.
16. W.E. Ranz and W.R. Marshall, Jr.: *Chem. Eng. Progr.,* 1952, vol. 48 (3), pp. 141-46.
17. A.H. Dilawari, J. Szekely, J. Batdorf, R. Detering, and C.B. Shaw: *Plasma Chem. Plasma Processing,* 1990, vol. 10, pp. 321-37.
18. N. El-Kaddah, J. McKelliget, and J. Szekely: *Metall. Trans. B,* 1984, vol. 15B, pp. 59-70.
19. W. Krebs: Dr.-Ing. Dissertation, University of Karlsruhe, Karlsruhe, 1995, (in German).
20. D.P.H. Hasselman, L.F. Johnson, L.D. Bensten, R. Syed, H.L. Lee, and M.V. Swain: *Am. Ceramic Soc. Bull.,* 1987, vol. 66, pp. 799-806.
21. *Handbook of Chemistry & Physics,* 65th ed., CRC, Boca Raton, FL, 1984
22. B.M. Cetegen and W. Yu: *J. Thermal Spray Technol.,* 1999, vol. 8(1), pp. 57–67.